# Gating-like Motions and Wall Porosity in a DNA Nanopore Scaffold Revealed by Molecular Simulations

*Vishal Maingi[1], Mickaël Lelimousin[1,2], Stefan Howorka[3], Mark. S. P. Sansom[1] \**

[1]Department of Biochemistry, University of Oxford, South Parks Road, Oxford OX1 3QU, Oxford, United Kingdom

[2](current address) CERMAV, Université Grenoble Alpes and CNRS, BP 53, F-38041 Grenoble Cedex 9, France

[3]Department of Chemistry, Institute of Structural Molecular Biology, University College London, London WC1H 0AJ, England, United Kingdom


\*to whom correspondence should be addressed.
Email          mark.sansom@bioch.ox.ac.uk
Direct:        +44 (0)1865-613306
PA:            +44 (0)1865-613212

**ABSTRACT**

Recently developed synthetic membrane pores composed of folded DNA enrich the current range of natural and engineered protein pores and of non-biogenic channels. Here we report all-atom molecular dynamics simulations of a DNA nanotube (DNT) pore scaffold to gain fundamental insight into its atomic structure, dynamics, and interactions with ions and water. Our multiple simulations of models of DNTs that are composed of a six-duplex bundle lead to a coherent description. The central tube lumen adopts a cylindrical shape while the mouth regions at the two DNT openings undergo gating-like motions which provide a possible molecular explanation of a lower conductance state observed in our previous experimental study on a membrane-spanning version of the DNT (_ACS Nano._ 2015, 9, 1117-26). Similarly, the central nanotube lumen is filled with water and ions characterized by bulk diffusion coefficients while the gating regions exhibit temporal fluctuations in their aqueous volume. We furthermore observe that the porous nature of the walls allows lateral leakage of ions and water. This study will benefit rational design of DNA nanopores of enhanced stability of relevance for sensing applications, of nanodevices with tunable gating properties that mimic gated ion channels, or of nanopores featuring defined permeation behavior.

## INTRODUCTION

Nanopores can be formed in biological (i.e. lipid-bilayer) membranes, by a variety of materials, both biological and synthetic [1]. Membrane nanopores have been shown to be formed by carbon nanotubes [2], synthetic molecular assemblies [3], and cyclic peptides [4], in addition to biological pore-forming proteins such as porins [5] and α-hemolysin [6], and bundles of α-helices [7]. Nanopores are of importance not only in terms of enabling exploration of fundamental aspects of solute transport at the nanoscale [8], but also because of their potential applications in biotechnology [9] and biomedicine [10]. For example, they have been used as stochastic sensors [11, 12], and for the translocation of proteins [13] or nucleic acids [14, 15]. In particular, protein nanopores form the basis of new developments in next generation sequencing of genomic DNA [16].

Despite advances in design of novel protein nanopores [17], there is a need to expand the range of materials which may be used to design new membrane-spanning nanopores, allowing controlled pore selectivity and gating. Nucleic acids have recently been shown to constitute suitable building blocks to form novel nanopore scaffolds [18-22]. DNA nanotubes (DNTs) once suitably chemically derivatized to aid insertion into lipid bilayers have shown to function as nanopores in both artificial and cell membranes [20-22], thus offering novel platforms for biomimetic ion transport and for possible therapeutic applications [23].

The design and synthesis of DNTs is aided by the principles of DNA self-assembly and DNA origami [18, 19, 24-27]. Functionalization of the resultant DNTs with hydrophobic lipid anchors is essential to successfully embed the nanopores in membranes [20, 21, 28]. Experimental studies into their conductance properties established that the DNA pores exhibit two voltage-dependent conductance states [29]. Low transmembrane-voltages favors a stable high-conductance level, which corresponds to an unobstructed DNA pore, while higher voltages lead to a low-conductance state possibly caused by electric-field-induced changes of the DNA pore conformation. The detailed molecular reason for the two state switching could, however, not be determined due to lack of atomistic insight. An investigation of DNT's conformational dynamics could help settle this question. Examining the interactions of DNTs with ions and water, will also improve our fundamental understanding of the permeation properties and aid the development of novel DNT structures of designed function.

Molecular modelling and simulations can provide important insights into the sub-nanoscale structure and function of nanopores [8]. Molecular dynamics (MD) simulations have also been used to

reveal aspects of the mechanical properties of DNA-origami array structures [30]. MD simulations have also been performed to explore the ionic conductivity and structural deformation of DNA origami nanoplates in an electric field [31]. A recent examination of DNT structures by MD simulations suggested that DNTs formed by 6 DNA helix bundles may be more stable than those formed by 8-helix bundles [32]. However we still lack a complete understanding of the fundamental conformational dynamics of DNTs and of their interactions with ions and water, which will aid biomimetic design of novel features into such pores.

Here, we report all-atom MD simulations of a synthetic 6-helix DNT structure that has previously been shown to form a scaffold for ion permeable nanopores in membranes (Fig. 1A) [21]. Our analysis suggests that the central core of DNT is structurally stable while the terminal regions at two pore openings exhibit a greater degree of flexibility. The intrinsic gating-like behaviour seen at the mouths of the pore could either be exploited to produce nanodevices with predictable on-off states, or, alternatively, guide the engineering of pores with reduced conformational dynamics. The walls of the DNT are shown to be 'leaky' to ions and water, which will influence design of permeation and selectivity properties of DNA-based nanopores. Our study offers atomic insights into structure, dynamic and permeation of DNTs and hence constitutes an important advance that will guide rational biomimetic design.

**RESULTS AND DISCUSSION**

*Structure and stability of the DNT models.*

The DNT in this study [21] features a 6-helix scaffold composed of 14 strands (Fig. 1B). Following the principles of DNA origami, six oligonucleotides (Fig. 1B, yellow) run parallel to the duplexes while eight strands form short inter-duplex cross-overs to ensure the cohesion of the nanostructure. Two initial all-atom models were built (see SI Methods and Fig. S1 for details) with an interhelix spacing $d$ of either 18 or 20 Å (Fig. 1C). These two initial models ($d$ = 18 or 20 Å) were used as starting structures for four MD simulations, ranging in duration from ca. 150 to 500 ns (Table 1) of the DNT immersed in a 1M KCl solution. In these four simulations we varied the simulation conditions in order to explore the robustness of the conclusions derived from the subsequent analysis.

Analysis of the no-H atom RMSDs suggested that all four simulations equilibrated after 60 ns of simulation, to an RMSD relative to their respective average structures of ca. 4Å (SI Fig. S4). Structural stability of the models was confirmed by analysis of hydrogen-bonds between the base pairs within the DNT structure (SI Fig. S5). Therefore, all properties further investigated were

4

analysed from 60 ns to the end of the simulations. In all four simulations, the inter-helix spacing converged to $d = 24 \pm 1$Å, and the hexagonal shape of the central nanopore was retained (see SI Methods and Table S1 for details). So, in the subsequent analyses we will focus mainly on simulation DNT1 (Fig. 1D). Final snapshots and further analysis of the other models are provided in the Supporting Information (SI Fig. S6).

*Conformational dynamics of DNTs.*

Understanding the conformation and dynamics of DNTs is of interest in the context of designing DNT-based nanopores of defined structural stability or flexibility. To provide an overview of DNT dynamics we calculated the root mean square fluctuation (RMSFs) of the phosphorous atom positions, relative to the average structures over the equilibrated part of the simulations (i.e. after 60 ns). We observed low RSMF values in the central section of the DNT (regions G2 to G5) compared to those calculated for the mouth regions, G1 and G6, of the nanopore (Fig. 2ABC; also SI Fig. S7). Phosphorous atoms at the Holliday junctions, mainly located between G2 and G5, did not show large local motions (SI Fig. S8), indicative of overall nanopore stability. In particular the G4 region where chemical modifications have been made to provide a hydrophobic belt [21] showed relatively small fluctuations.

The flexibility observed in groups G1 and G6 is suggestive of motions which might result in possible gating at the mouths of the DNT. To explore this further we performed principal component analysis (PCA) to the major collective motions of the DNT backbone observed during the simulations. The first eigenvector identified through this analysis (Fig. 2D and SI Fig. S9, and SI movie S17) suggests a 'breathing motion' at the mouth regions of the DNT, *i.e.* the nanopore in regions G1 and G6 may successively expand and shrink. We identified two subgroups at the DNT termini that lacked staple strands, which could rationalize the motions observed by PCA. These subgroups were defined as G1a and G1b, and as G6a and G6b (Fig. 2A and SI Fig. S10). We explored possible correlations between motions at the two termini, i.e. between the G1a-G1b and the G6a-G6b distances (SI Fig. S11 and S12). This analysis did not reveal any significant correlations, suggesting that the gating motions at the two ends of the nanopore are independent of one another.

*Nanopore radius profiles*

We next examined the radius profile along the length of the nanotube (Fig. 3AB) to follow how the DNT structure changes in the simulations as well as to quantify the consequences of the pore dynamics. The initial model showed a fairly flat pore radius profile, with an average pore radius of

ca. 9 Å for DNT1 and DNT4 ($d$ = 20 Å) and of ca. 7 Å for DNT2 and DNT3 ($d$ = 18 Å). In all four simulations the central (regions G2 to G5) pore radius increased to ca. 10 Å, consistent with convergence on a equilibrium value of $d$ = 24 Å for the inter-helix spacing. In all four simulations a degree of narrowing at one (G1) or other (G6) mouth of the pore was observed, consistent with the suggestions of gating-like motions at the mouths of the pore discussed above. Thus in DNT1 and DNT4, both starting from the $d$ = 20 Å model, the average mouth radius dropped to ca. 5.5 Å at the G1 end and to ca. 7.5 Å at the G6 end respectively (Fig. 3AB). In order to characterize the gating motions at the pore mouths we calculated the pore radius profile as a function of simulation time e.g. for DNT1 and DNT4 (Fig. 3CD). Detailed inspection suggested multiple time dependent fluctuations in the pore radius. To further analyse such possible gating-like events we analysed the minimum pore radius as a function of time for both the G1 end (-70 to -30 Å) and the G6 end (30 to 70 Å) of the DNT (Fig. 4AB). This revealed fluctuations in these minimum radii, which we classified as either O (open-like) or C (closed-like) using a simple 6 Å threshold radius (based on consideration of the  radii of hydrated ions). This simple analysis yields a signal-like trace of the transitions of the pore between the O and C states (shown in Fig. 4CD for DNT1 and DNT4 respectively), revealing multiple transitions during the course of the simulations. For example, From this analysis, for DNT1 (Fig. 4C), we observe a dynamic narrowing/closure of the G6 gate which re-opens at ca. 100 ns and remains open for the rest of the simulation. In contrast the G1 gate is partly closed at the start and then more fully closes (and remains closed) after ca. 100 ns with short transient re-openings from 130-140ns. For the longer (500 ns; Fig. 4D) DNT4 simulation we observe multiple brief closures at the G1 mouth, alongside frequent stochastic switching between O and C at the G6 mouth of the nanopore. (Analysis for the DNT2 and DNT3 simulations other simulations are shown in SI Fig. S13, S14).

*Ions and Water in the DNT Nanopore*

The temporal evolution of the lumen dimensions offers an opportunity to investigate the effect on ions and water within the DNT. As discussed above (Fig. 3), in the central lumen region the nanopore radius is ca. 10 Å and shows only small fluctuations. Consequently there are no large temporal variations in the density of water or of ions in the lumen. In contrast, the mouths of the DNT are narrower and undergo dynamic changes over the course of the simulation. We therefore calculated the numbers of both ion species and of water molecules along the pore axis, focussing especially (in simulation DNT1) on the G1 mouth of nanopore (Fig. 5AB). We clearly observe that as the G1 mouth region narrows (after ca. 100 ns), the number of both ions and water decreases in this region (Fig. 5AB). This effect is most obvious for the Cl$^-$ ions due to their electrostatic repulsion by the phosphate groups of the DNT backbone.

We also determined the diffusion coefficients of ions and water in the lumen along the nanopore axis (Fig. 5C). The diffusion coefficients were derived from mean square displacements of ions and water locally within grid volumes along the DNT (see SI and Fig. S3 for further details). Along the central region of the pore (from G2 to G5) constant diffusion coefficients were observed for water (ca. 3 x $10^{-5}$ cm$^2$ s$^{-1}$) and ions (ca. 2 x $10^{-5}$ cm$^2$ s$^{-1}$). These are just a little lower than the corresponding values in bulk solution (see Fig. 6C and below). In the constricted G1 mouth these diffusion coefficients were decreased approximately twofold, this effect being most marked for K$^+$ ions. These findings indicate that even the incomplete 'closure' of the G1 gate at the mouth of the pore significantly slows diffusive motions of both ion and solvent, consistent with a likely effect on ionic conductance.

By integrating the pore radius profiles, we were able to compare the volumes of the nanopore for the four simulations. This is consistently ca. 1.1 x $10^5$ Å$^3$ for all four simulations (SI. Fig S15). Similar calculation for the numbers of both ionic species in lumen (Table 2 and SI Fig S16) yielded an overall selectivity for cations (K$^+$) over anions (Cl$^-$), of ca. 2.4:1, as anticipated given the anionic nature of DNA.

*Porous Walls.*

Visual inspection of the simulations indicated a degree of penetration of both species of ions and of water molecules into the walls of the DNT nanopore. We quantified this by calculation of cylindrical radial distribution functions (see SI Methods and Fig. S2A) of ions, of water molecules, and of the phosphorous atoms of the DNA along the DNT core region G2-G5 (Fig. 6AB). (Note the dynamic G1 and G6 pore mouth regions were excluded from this analysis). Interestingly in the very centre of the lumen of the nanopore the number densities of ions and water densities are very similar to those in the bulk solution, which thus shows only weak cation selectivity. However, adjacent to the walls the cation:anion selectivity rises to >3:1. It can be seen that there are significant numbers of K$^+$ ions in the walls of the nanopore, that the water density falls within the walls by ca. 3x on average, and that there are even some Cl$^-$ ions within the wall region.

The presence of ions and water within the wall of the DNT nanopore shows the soft nature of this interface. We therefore analysed diffusion coefficients of ions and water as a function of radius (again along the DNT core region G2-G5; Fig. 6C). Within the wall region, the diffusion coefficients are reduced by ca. 2.5 fold, which is perhaps less than we might have anticipated. This directly reveals the porous nature of the wall of the DNT nanopore.

Returning to visualization of the simulations in this context, detailed examination of simulation snapshots (Fig. 7A) reveals 'sideways leaks' in the wall of the nanopore which can accommodate ions and water molecules. We therefore analysed the spatial distribution (see SI Methods and Fig. S2B), of diffusion coefficients of ions and could see a clear (negative) correlation between the local ionic diffusion coefficients and the local density of atoms from the DNA molecules of the DNT (Fig. 7B). This confirms the sponge-like nature of the walls of the DNT nanopore, with penetration of water and ions into the less densely packed regions of the pore wall.

**CONCLUSIONS.**

In this study we performed all-atom MD simulations of a model DNT structure that has previously been shown to form ion conducting nanopores when embedded within a lipid bilayer membrane [21]. Comparing our four simulations, we demonstrated this model is robust and stable on a sub-microsecond timescale in 1 M KCl solution. The four simulations provide a coherent description of the structure and the conformational dynamics of the DNT. The central lumen does not undergo large fluctuations but the terminal regions of the DNT exhibit dynamic flexibility that provides a gating-like motion at the mouths of the pore on a sub-microsecond timescale. Partial closure of these gate-like regions results in significant reduction in ion and water diffusion at either mouth of the nanopore. The gating-like motion in the simulations offers a plausible explanation for the experimentally observed voltage-induced switching from a low transmembrane-voltage high-conductance level to a high voltage low-conductance state [29]. Prior to the simulations, the molecular nature of the gating was unclear and could include an electric-field-induced fraying of DNA duplexes, flipping of DNA loops at the pore entrances, conformational alterations in the overall duplex structure or the relative position between duplexes. Our simulations narrow down the options and suggest that the intrinsic gating-like behaviour at the pore mouth regions is the most plausible mechanism for the experimentally observed conductance switching. Such gating-like motions would modulate an underlying transport mechanism based on diffusion of ions and water through the central pore. The comparison between experimental current fluctuations and simulated gating-like motions has, however, to take account of differences. For example, the simulations were not performed for a membrane-embedded DNT under transmembrane voltage as in the ionic current measurements. In addition, the time scales for the simulations are (as is generally the case for MD simulations) much shorter than the temporal resolution of the conductance experiments and observed gating kinetics. Nevertheless, it is valid to assume that experimentally observed current blockades involve the structural flexibility of the pore-mouth regions, which may be further amplified in extent by the transmembrane voltage.

These fundamental insights into pore dynamics can also aid the design of pores of defined structural and functional properties. For example, the known location for intrinsic gating of DNT's could be exploited to design biomimetic nanodevices that undergo tuneable trigger-dependent conductance changes similar to natural ion channels. By contrast, the knowledge of a stable pore lumen and flexible termini can serve as a structural guide to reengineer DNA nanopores. For sensing applications, the pore should be void of major intrinsic conformational changes which would interfere with the binding or detection of passing analytes. Clearly, the flexible pore termini could be altered to prepare a scaffold of increased stability.

The nanopore is, as anticipated, cation selective, with strong selectivity at the (inner) walls of the nanopore, but little selectivity in the centre of the pore lumen. Perhaps surprisingly the walls of the DNT structure are shown to be soft and porous, allowing lateral leakage of ions and water molecules. This is in marked contrast with e.g. CNT [33] or protein (β-barrel) [8] nanopores, providing an interesting feature which may be exploited in future DNT nanopore designs.

These studies in particular allow us to probe the diffusive behaviour of ions within the pore formed by a DNA-origami structure. Due to its highly charged nature, DNA interacts strongly with ions. For example, the structure of dsDNA is influenced by ions [34-36]. Within DNA-origami constructs, which are made up of dense assemblies of DNA strands, we might expect effects of ionic concentration on DNT structure. For example changes in ionic concentration have been shown to modify the structure and the behaviour of DNA-plate architectures [31]. In the current study we have employed a single ionic concentration, chosen to match that used in functional experiments [21], but future studies will explore the effects of changes in ionic species and concentration. It will also be of interest in the future to explore the effects of hydrophobic derivatization of DNTs, as this is required to stabilize such nanopores within a lipid bilayer environment. Preliminary simulation studies using the MARTINI coarse-grained model [37] suggest that hydrophobic derivatization is sufficient to maintain a DNT stably spanning a simple lipid bilayer, but more detailed studies will be required to fully explore the interplay of lipids and DNA in this system.

**METHODS**.

*Modelling.*

An initial model was constructed starting from six B-DNA double helices placed on a hexagonal pattern with inter-helix spacing $d$ = 18 or 20 Å. Junctions were introduced by breaking and re-

joining the strands as in the experimental design [21]. This scaffold was then used to generate an initial DNT model that was obtained with 14 single strands of DNA (see SI Methods and Fig. S1 for details).

*Simulations.*

The four simulations are summarized in Table 1. AMBER12 CUDA version [38, 39] (http://ambermd.org/) was employed for DNT1, DNT2 and DNT3 simulations using the AMBERff99+parmbasc0 force field [40]. Simulation DNT4 was performed using GROMACS 4.6.5 [41] (www.gromacs.org) and the CHARMM36 force field [42] in order to compare and assess the results using different force fields used. The initial DNT1 ($d = 20$ Å) and DNT2 ($d = 18$ Å) models were solvated with a 12 Å buffer of water using the TIP3P model [43] in a truncated octahedral box of with KCl [44] at a concentration of 1M. Additional $K^+$ ions were added to neutralize the phosphate groups of the DNT backbone.

The solvated systems were subject to steepest descents followed by conjugate gradient minimization with harmonic constraints applied to the position of the DNT atoms. The energy-minimization was repeated several times, lowering progressively the force constants from 500 kcal $mol^{-1}Å^{-2}$ down to 20 kcal $mol^{-1} Å^{-2}$. The systems were then slowly heated while maintaining weak harmonic constraints on the DNT atom positions. At each temperature between 0 K and 300 K molecular dynamics (MD) simulation was performed in the NVT ensemble. The temperatures were kept constant using a Berendsen thermostat [45] and a relaxation time of 0.5 ps. A time step of 2 fs was used to integrate the equations of motions, with the SHAKE algorithm. During this heating process, inter-helix interactions were maintained using the EMAP method [46] which helped to maintain the internal geometry while at the same time allowing inter-helix interactions. This slow relaxation was carried over 1ns. This strategy successfully removed strong electrostatic repulsions between helices from the initial hexagonal DNT models. The heating was followed by 20 ns of MD simulation in the NVT ensemble at 300 K with weaker harmonic positional constraints (10 kcal $mol^{-1} Å^{-2}$) applied to the DNT atoms. This allowed equilibration of the positions of ions around the DNT surface. The harmonic constraints were then slowly removed by consecutive runs of 1 ns in the NVT ensemble (force constants of 10, 5 and then 1 kcal $mol^{-1} Å^{-2}$). Finally the extended, unrestrained MD simulation was performed in the NPT ensemble with a Berendsen thermostat and barostat [45] with heat bath coupling time of 1 ps and pressure relaxation time of 2 ps. A cut-off of 9 Å was used to treat short-range van der Waals interactions. The particle mesh Ewald (PME) method [47] was used for electrostatic interactions with a real-space cut-off of 9 Å, an order 4 cubic B-spline interpolation and direct space cutoff tolerance set being $10^{-4}$.

For DNT3 a slightly different protocol was adopted. The DNT2 structure obtained after the EMAP step described above, was subjected to the same subsequent NVT and NPT simulations but using a Langevin thermostat with collision frequency 1 ps$^{-1}$. For the DNT4 simulation, the DNT1 structure obtained after the EMAP step was used but switching to the CHARMM36 forcefield. The DNT4 model was solvated with a 24 Å buffer of TIP3P waters in a truncated octahedral box. The simulation protocol was the same as for the DNT1 simulation but with a Langevin thermostat.

*Analysis.*

Analyses were performed with locally-written PERL scripts, AMBERTools [48] and GROMACS utilities. Images were produced using VMD [49] and CHIMERA [50]. Pore radius profiles were calculated using HOLE [51]. Diffusion coefficients of ions and water molecules were calculated from the mean square displacements (MSD) of atoms, as *D = MSD/6t*. Detailed information about the analysis protocols is provided in Supporting Information, SI Methods.

**ACKNOWLEDGEMENTS**

**SUPPORTING INFORMATION AVAILABLE:**

Supporting methodological information, figures, and a movie are available free of charge via the

Internet at http://pubs.acs.org.

**REFERENCES**:

(1)    Tagliazucchi, M.; Szleifer, I. Transport mechanisms in nanopores and nanochannels: can we mimic nature? *Materials Today* **2015**, *18*, 131-142.

(2)    Liu, L.; Yang, C.; Zhao, K.; Li, J. Y.; Wu, H. C. Ultrashort single-walled carbon nanotubes in a lipid bilayer as a new nanopore sensor. *Nature Comma.* **2013**, *4*.

(3)    Chui, J. K. W.; Fyles, T. M. Ionic conductance of synthetic channels: analysis, lessons, and recommendations. *Chem. Soc. Rev.* **2012**, *41*, 148-175.

(4)    Ghadiri, M. R.; Granja, J. R.; Buehler, L. K. Artificial transmembrane ion channels from self-assembling peptide nanotubes. *Nature* **1994**, *369*, 301-304.

(5)    Chen, M.; Khalid, S.; Sansom, M. S. P.; Bayley, H. Outer membrane protein G: engineering a quiet pore for biosensing. *Proc. Natl. Acad. Sci. USA* **2008**, *105*, 6272-6277.

(6)    Song, L.; Hobaugh, M. R.; Shustak, C.; Cheley, S.; Bayley, H.; Gouaux, J. E. Structure of staphylococcal α-hemolysin, a heptameric transmembrane pore. *Science* **1996**, *274*, 1859-1866.

(7)    Lear, J. D.; Wasserman, Z. R.; DeGrado, W. F. Synthetic amphiphilic peptide models for protein ion channels. *Science* **1988**, *240*, 1177-1181.

(8)    Trick, J. L.; Aryal, P.; Tucker, S. J.; Sansom, M. S. P. Molecular simulation studies of hydrophobic gating in nanopores and ion channels. *Biochem. Soc. Trans,* **2015**, *43*, 146-150.

(9)    Stoloff, D. H.; Wanunu, M. Recent trends in nanopores for biotechnology. *Curr. Opin. Biotechnol.* **2013**, *24*, 699-704.

(10)   Wang, Y.; Zheng, D. L.; Tan, Q. L.; Wang, M. X.; Gu, L. Q. Nanopore-based detection of circulating microRNAs in lung cancer patients. *Nature Nanotech.* **2011**, *6*, 668-674.

(11)   Gu, L. Q.; Braha, O.; Conlan, S.; Cheley, S.; Bayley, H. Stochastic sensing of organic analytes by a pore-forming protein containing a molecular adapter. *Nature* **1999**, *398*, 686-690.

(12)   Howorka, S.; Siwy, Z. Nanopore analytics: sensing of single molecules. *Chem. Soc. Rev.* **2009**, *38*, 2360-2384.

(13)   Yusko, E. C.; Johnson, J. M.; Majd, S.; Prangkio, P.; Rollings, R. C.; Li, J. L.; Yang, J.; Mayer, M. Controlling protein translocation through nanopores with bio-inspired fluid walls. *Nature Nanotechnol.* **2011**, *6*, 253-260.

(14)   Kasianowicz, J. J.; Brandin, E.; Branton, D.; Deamer, D. W. Characterization of individual polynucleotide molecules using a membrane channel. *Proc. Natl. Acad. Sci. USA* **1996**, *93*, 13770-13773.

(15)   Howorka, S.; Cheley, S.; Bayley, H. Sequence-specific detection of individual DNA strands using engineered nanopores. *Nature Biotech.* **2001**, *19*, 636-639.

(16)   Loman, N.; Quick, J.; Simpson, J. A complete bacterial genome assembled de novo using only nanopore sequencing data. *Nature Methods* **2015**, *doi:10.1038/nmeth.3444*.

(17)   Thomson, A. R.; Wood, C. W.; Burton, A. J.; Bartlett, G. J.; Sessions, R. B.; Brady, R. L.; Woolfson, D. N. Computational design of water-soluble alpha-helical barrels. *Science* **2014**, *346*, 485-488.

(18)   Langecker, M.; Arnaut, V.; Martin, T. G.; List, J.; Renner, S.; Mayer, M.; Dietz, H.; Simmel, F. C. Synthetic lipid membrane channels formed by designed DNA nanostructures. *Science* **2012**, *338*, 932-936.

(19)   Bell, N. A. W.; Engst, C. R.; Ablay, M.; Divitini, G.; Ducati, C.; Liedl, T.; Keyser, U. F. DNA origami nanopores. *Nano Lett.* **2012**, *12*, 512-517.

(20)   Burns, J. R.; Gopfrich, K.; Wood, J. W.; Thacker, V. V.; Stulz, E.; Keyser, U. F.; Howorka, S. Lipid-bilayer-spanning DNA nanopores with a bifunctional porphyrin anchor. *Angew. Chem. Int. Ed.* **2013**, *52*, 12069-12072.

(21)     Burns, J. R.; Stulz, E.; Howorka, S. Self-assembled DNA nanopores that span lipid bilayers. *Nano Lett.* **2013**, *13*, 2351-2356.

(22)     Burns, J. R.; Al-Juffali, N.; Janes, S. M.; Howorka, S. Membrane-spanning DNA nanopores with cytotoxic effect. *Angew. Chem. Int. Ed.* **2014**, *53*, 12466-12470.

(23)     Hernandez-Ainsa, S.; Keyser, U. F. DNA origami nanopores: an emerging tool in biomedicine. *Nanomed.* **2013**, *8*, 1551-1554.

(24)     Rothemund, P. W. K.; Ekani-Nkodo, A.; Papadakis, N.; Kumar, A.; Fygenson, D. K.; Winfree, E. Design and characterization of programmable DNA nanotubes. *J. Amer. Chem. Soc.* **2004**, *126*, 16344-16352.

(25)     Rothemund, P. W. K. Folding DNA to create nanoscale shapes and patterns. *Nature* **2006**, *440*, 297-302.

(26)     Mitchell, J. C.; Harris, J. R.; Malo, J.; Bath, J.; Turberfield, A. J. Self-assembly of chiral DNA nanotubes. *J. Amer. Chem. Soc.* **2004**, *126*, 16342-16343.

(27)     Hariri, A. A.; Hamblin, G. D.; Gidi, Y.; Sleiman, H. F.; Cosa, G. Stepwise growth of surface-grafted DNA nanotubes visualized at the single-molecule level. *Nature Chem.* **2015**, *7*, 295-300.

(28)     Gopfrich, K.; Zettl, T.; Meijering, A. E. C.; Hernandez-Ainsa, S.; Kocabey, S.; Liedl, T.; Keyser, U. F. DNA-tile structures induce ionic currents through lipid membranes. *Nano Lett.* **2015**, *15*, 3134-3138.

(29)     Seifert, A.; Gopfrich, K.; Burns, J. R.; Fertig, N.; Keyser, U. F.; Howorka, S. Bilayer-spanning DNA nanopores with voltage-switching between open and closed state. *ACS Nano* **2015**, *9*, 1117-1126.

(30)     Yoo, J.; Aksimentiev, A. In situ structure and dynamics of DNA origami determined through molecular dynamics simulations. *Proc. Natl. Acad. Sci. USA* **2013**, *110*, 20099-20104.

(31)     Li, C. Y.; Hemmig, E. A.; Kong, J. L.; Yoo, J.; Hernandez-Ainsa, S.; Keyser, U. F.; Aksimentiev, A. Ionic conductivity, structural deformation, and programmable anisotropy of DNA origami in electric field. *ACS Nano* **2015**, *9*, 1420-1433.

(32)     Joshi, H.; Dwaraknath, A.; Maiti, P. K. Structure, stability and elasticity of DNA nanotubes. *Phys. Chem. Chem. Phys.* **2015**, *17*, 1424-1434.

(33)     Garcia-Fandino, R.; Sansom, M. S. P. Designing biomimetic pores based on carbon nanotubes. *Proc. Natl. Acad. Sci. USA* **2012**, *109*, 6939-6944.

(34)     Egli, M. DNA-cation interactions: Quo vadis? *Chemistry & Biology* **2002**, *9*, 277-286.

(35)     Varnai, P.; Zakrzewska, K. DNA and its counterions: a molecular dynamics study. *Nucleic Acids Res.* **2004**, *32*, 4269-4280.

(36)     Gueroult, M.; Boittin, O.; Mauffret, O.; Etchebest, C.; Hartmann, B. $Mg^{2+}$ in the major groove modulates B-DNA structure and dynamics. *PLoS One* **2012**, *7*.

(37)     Marrink, S. J.; Tieleman, D. P. Perspective on the Martini model. *Chem. Soc. Rev.* **2013**, *42*, 6801-6822.

(38)     Pearlman, D. A.; Case, D. A.; Caldwell, J. W.; Ross, W. S.; Cheatham, T. E.; Debolt, S.; Ferguson, D.; Seibel, G.; Kollman, P. Amber, a package of computer-programs for applying molecular mechanics, normal-mode analysis, molecular-dynamics and free-energy calculations to simulate the structural and energetic properties of molecules. *Comp. Phys. Comm.* **1995**, *91*, 1-41.

(39)     Salomon-Ferrer, R.; Gotz, A. W.; Poole, D.; Le Grand, S.; Walker, R. C. Routine microsecond molecular dynamics simulations with AMBER on GPUs. 2. explicit solvent particle mesh Ewald. *J. Chem. Theor. Comp.* **2013**, *9*, 3878-3888.

(40)     Perez, A.; Marchan, I.; Svozil, D.; Sponer, J.; Cheatham, T. E.; Laughton, C. A.; Orozco, M. Refinenement of the AMBER force field for nucleic acids: Improving the description of alpha/gamma conformers. *Biophys. J.* **2007**, *92*, 3817-3829.

(41)    Hess, B.; Kutzner, C.; van der Spoel, D.; Lindahl, E. GROMACS 4: algorithms for highly efficient, load-balanced, and scalable molecular simulation. *J. Chem. Theor. Comp.* **2008**, *4*, 435-447.

(42)    Hart, K.; Foloppe, N.; Baker, C. M.; Denning, E. J.; Nilsson, L.; MacKerell, A. D. Optimization of the CHARMM additive force field for DNA: improved treatment of the BI/BII conformational equilibrium. *J. Chem. Theor. Comp.* **2012**, *8*, 348-362.

(43)    Jorgensen, W. L.; Chandresekhar, J.; Madura, J. D.; Impey, R. W.; Klein, M. L. Comparison of simple potential functions for simulating liquid water. *J. Chem. Phys.* **1983**, *79*, 926-935.

(44)    Joung, I. S.; Cheatham, T. E. Determination of alkali and halide monovalent ion parameters for use in explicitly solvated biomolecular simulations. *J. Phys. Chem. B* **2008**, *112*, 9020-9041.

(45)    Berendsen, H. J. C.; Postma, J. P. M.; van Gunsteren, W. F.; DiNola, A.; Haak, J. R. Molecular dynamics with coupling to an external bath. *J. Chem. Phys.* **1984**, *81*, 3684-3690.

(46)    Wu, X. W.; Subramaniam, S.; Case, D. A.; Wu, K. W.; Brooks, B. R. Targeted conformational search with map-restrained self-guided Langevin dynamics: Application to flexible fitting into electron microscopic density maps. *J. Struct. Biol.* **2013**, *183*, 429-440.

(47)    Darden, T.; York, D.; Pedersen, L. Particle mesh Ewald - an N.log(N) method for Ewald sums in large systems. *J. Chem. Phys.* **1993**, *98*, 10089-10092.

(48)    Roe, D. R.; Cheatham, T. E. PTRAJ and CPPTRAJ: software for processing and analysis of molecular dynamics trajectory data. *J. Chem. Theor. Comp.* **2013**, *9*, 3084-3095.

(49)    Humphrey, W.; Dalke, A.; Schulten, K. VMD - Visual Molecular Dynamics. *J. Molec. Graph.* **1996**, *14*, 33-38.

(50)    Pettersen, E. F.; Goddard, T. D.; Huang, C. C.; Couch, G. S.; Greenblatt, D. M.; Meng, E. C.; Ferrin, T. E. UCSF Chimera - a visualization system for exploratory research and analysis. *J. Comp. Chem.* **2004**, *25*, 1605-1612.

(51)    Smart, O. S.; Neduvelil, J. G.; Wang, X.; Wallace, B. A.; Sansom, M. S. P. Hole: A program for the analysis of the pore dimensions of ion channel structural models. *J. Mol. Graph.* **1996**, *14*, 354-360.

**TABLES**

**Table 1:** Description of the all-atom MD simulations performed to obtain the four DNT models (see also Methods).

| Model | Initial Hexagon Length $d$ (Å) | All-atom Force Field | Temperature Control Scheme | Simulation Time (ns) |
|-------|-------|-------|-------|-------|
| DNT1 | 20 | AMBER parmbasc0 | Berendsen | 170 |
| DNT2 | 18 | AMBER parmbasc0 | Berendsen | 165 |
| DNT3 | 18 | AMBER parmbasc0 | Langevin | 115 |
| DNT4 | 20 | CHARMM36 | Langevin | 500 |

**Table 2**. Average equilibrium properties of the lumen region of the full-length DNT models. The ionic concentrations were calculated within a cylinder of radius 12 Å passing through the centre of the DNT (see SI Figures S15 and S16).

| Model | $V_{pore}$ ($10^3$ Å$^3$) | [K$^+$] (M) | [Cl$^-$] (M) |
|-------|---------------------------|-------------|--------------|
| DNT1  | $107 \pm 2.4$             | $1.93 \pm 0.14$ | $0.82 \pm 0.11$ |
| DNT2  | $110 \pm 3.3$             | $1.81 \pm 0.15$ | $0.87 \pm 0.13$ |
| DNT3  | $108 \pm 2.9$             | $1.82 \pm 0.16$ | $0.96 \pm 0.17$ |
| DNT4  | $115 \pm 4.5$             | $1.64 \pm 0.15$ | $0.68 \pm 0.14$ |

**FIGURES**
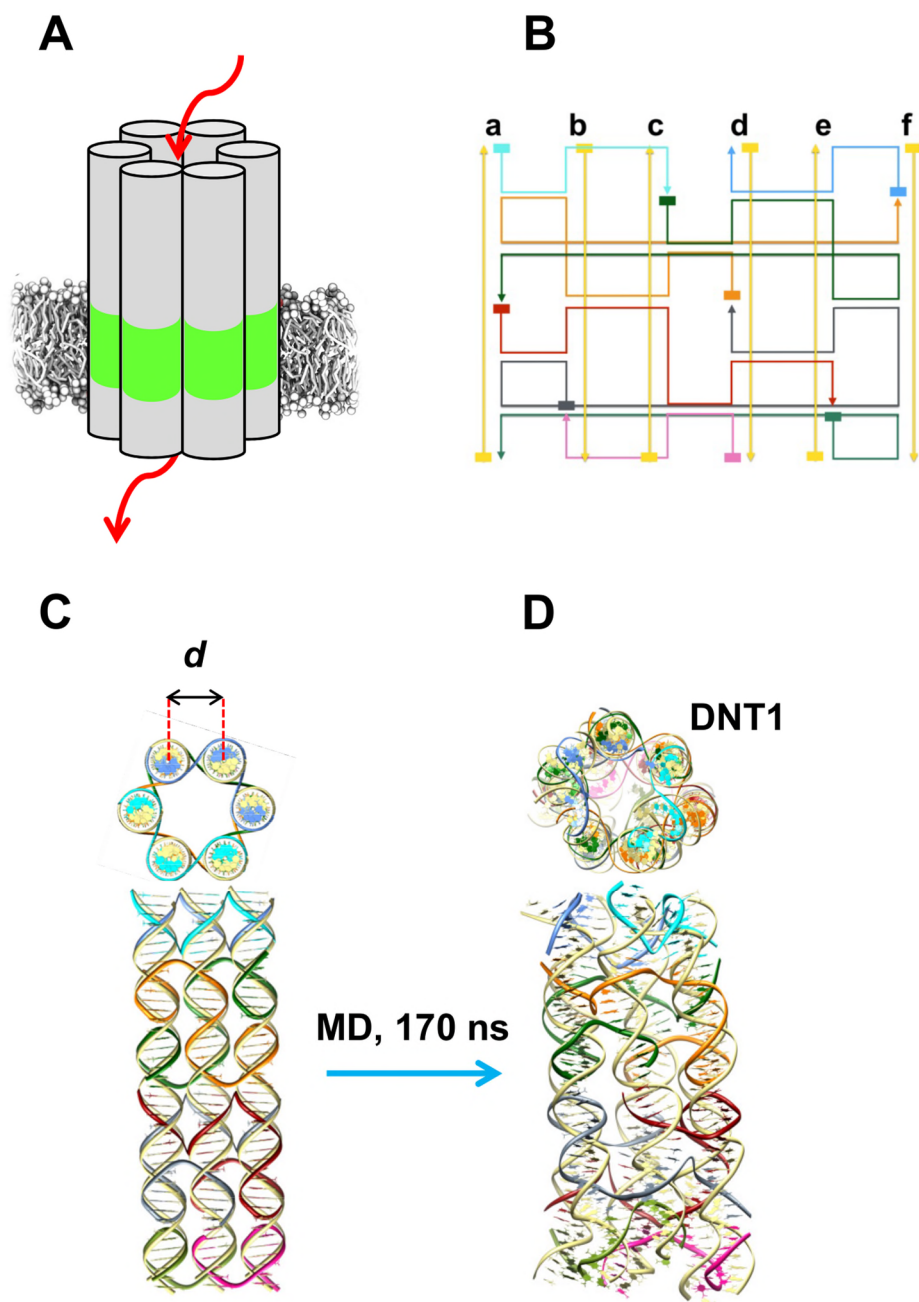


**Figure 1**. **Modelling the 6-helix DNT structure**.

**(A)** Schematic representation of a 6-helix DNT forming an ion permeable nanopore embedded in a lipid bilayer. DNT helices are represented by grey cylinders with the green regions corresponding to the hydrophobic surface band which stabilizes the nanopore within the hydrophobic core of the membrane. The lipid bilayer surrounding is shown in grey. **(B)** 2D representation of the DNT structure displaying the crossover points between the six dsDNA helices. The six scaffold strands are in yellow, whilst the eight staple strands in other colors. **(C)** Initial hexagonal bundle model for DNT. The distance *d* between adjacent helices was either 18 Å or 20 Å. The DNA strands are drawn using the same colour scheme as in **B**. **(D)** Structure of the DNT1 model after 170 ns of MD simulation.
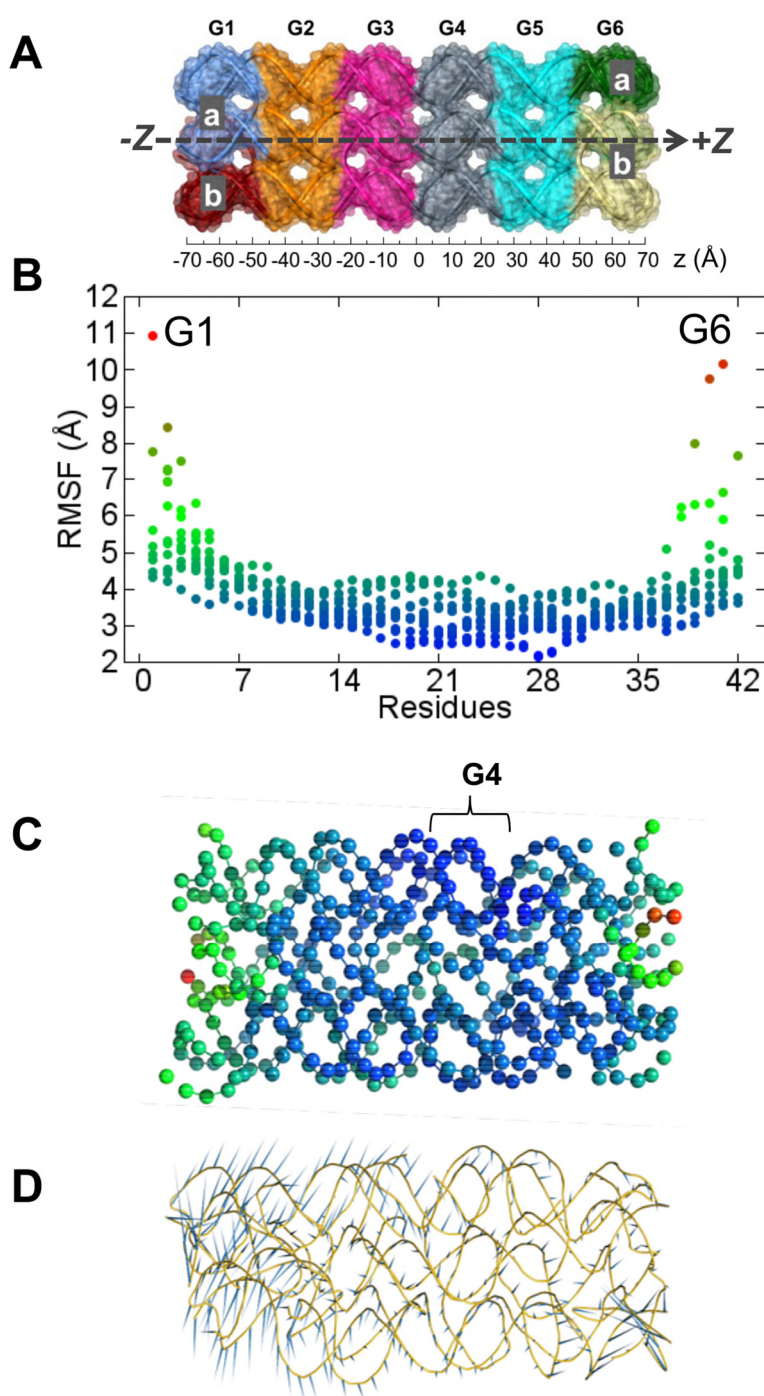
**Figure 2**: **Conformational dynamics of the DNT structure**.

**(A)** Definition of 6 regions of the DNT, from G1 to G6, with an equal length of 7 bases along the pore axis. These regions are based on crossover points where the folding of staple strands occurs. **(B)** Root mean square fluctuation (RMSF) values of phosphorous atoms along the pore axis of the DNT1 model. The DNT length consists of 42 bases, thus *X*-axis shows the base/residue number of along the pore. **(C)** Average structure from the DNT1 simulation, represented as phosphorous atoms coloured using the same RMSF scale as in **B**. The G4 region corresponds to the location of the hydrophobic band shown in Fig. 1A. **(D)** Backbone structure from the DNT1 simulation with the P-atom trace shown in yellow, and the blue arrows indicating the first eigenvector calculated by principal component analysis of the MD simulation (also see SI movie S17).
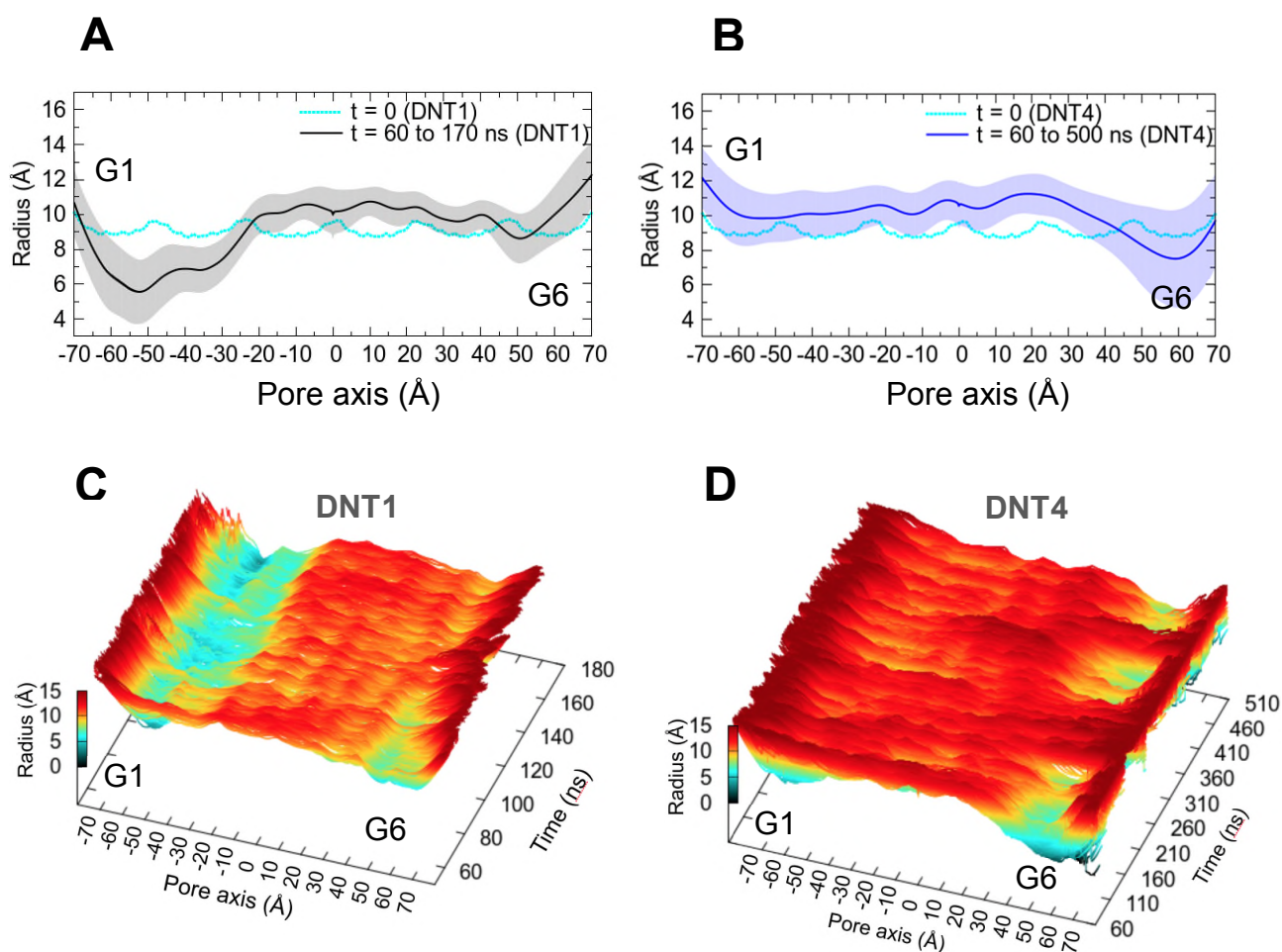
**A**



**B**

**C**

**D**

**Figure 3**: **Pore radius profile**.

**(A, B)** Pore radius profiles along the principal axis of the nanopore for the DNT1 and DNT4 simulations. The cyan line shows the radius profile of the initial model of the system (t = 0). The black line in **A** and blue line **B** represents the radius profile averaged over the equilibrated section of the simulations (t = 60 to 170 ns for DNT1 and t = 60 to 500 ns for DNT4), the corresponding grey and blue bands reporting the standard deviations. **(C, D)** The pore radius profiles of the DNT1 and DNT4 simulations are shown as a function of time as a combined heatmap and surface plot. This was obtained by juxtaposing radius profile curves averaged within 100 ps windows.
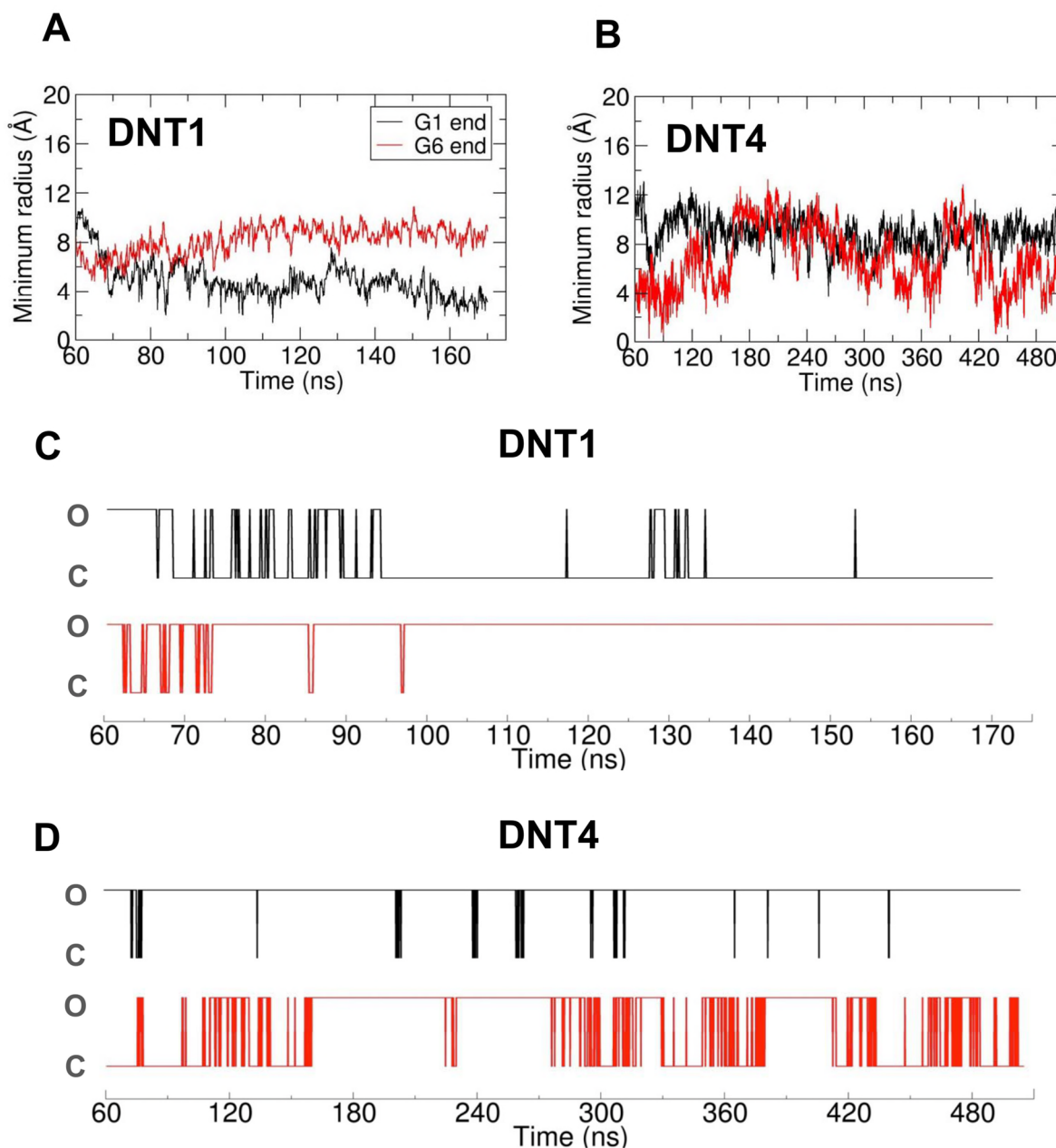
**Figure 4**:  **Minimum pore radii at the two ends of the nanopore.**

**(A, B)** Time evolution of the minimum pore radius as a function of time for the G1 end (-70 to -30 Å) and the G6 end (30 to 70 Å) of the nanopore for the DNT1 and DNT4 simulations. **(C, D)** Fluctuations in the minimum radii were used to classify the DNT as being either O (open-like) or C (closed-like) state, using a simple 6 Å threshold radius, yielding a signal-like trace of the transitions of the nanopore between the O and C states
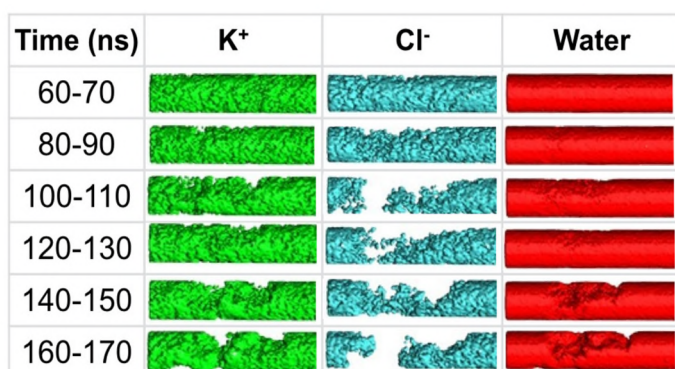
**A**



**B**


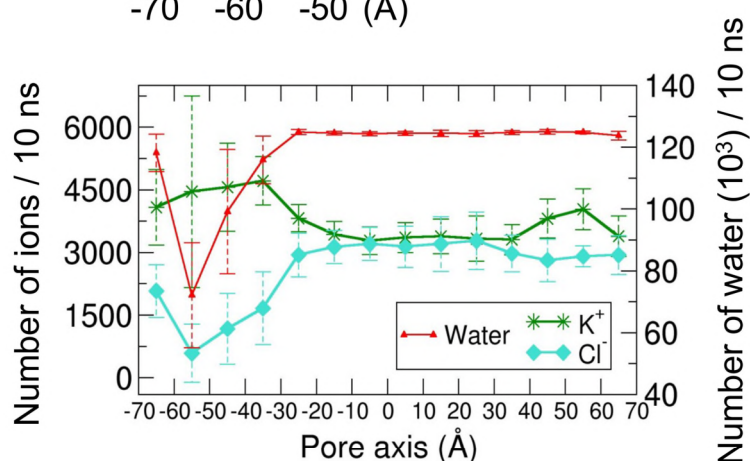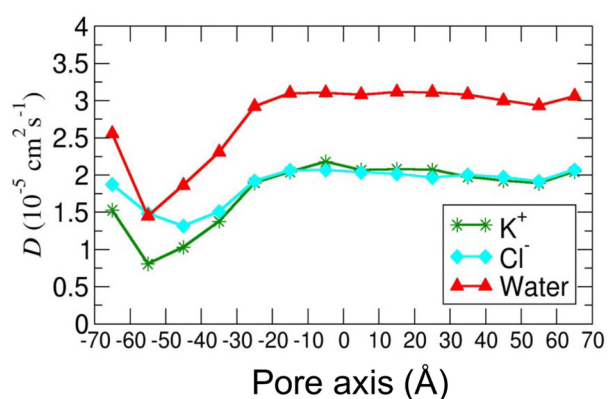
**C**



**Figure 5**: **Distribution and diffusion of ions and water along the pore axis**.
**(A)** Time-evolution of the distribution of $K^+$ ions, $Cl^-$ ions and water molecules in the G1-G2 region of the pore (shown for a central cylindrical volume of radius 5 Å) for consecutive intervals of the DNT1 simulation. **(B)** Average numbers of ions or waters per 10 ns frame along the central pore axis, calculated between 60 ns and 170 ns of the simulation. **(C)** Diffusion coefficient of $K^+$ and of $Cl^-$ and water molecules as a function of position along the pore axis of the DNT1 system calculated between 60 ns and 170 ns of the simulation (see SI Methods for details). For **B** and **C**, cylindrical grids of length 10 Å and radius 5 Å were constructed along the central pore axis.
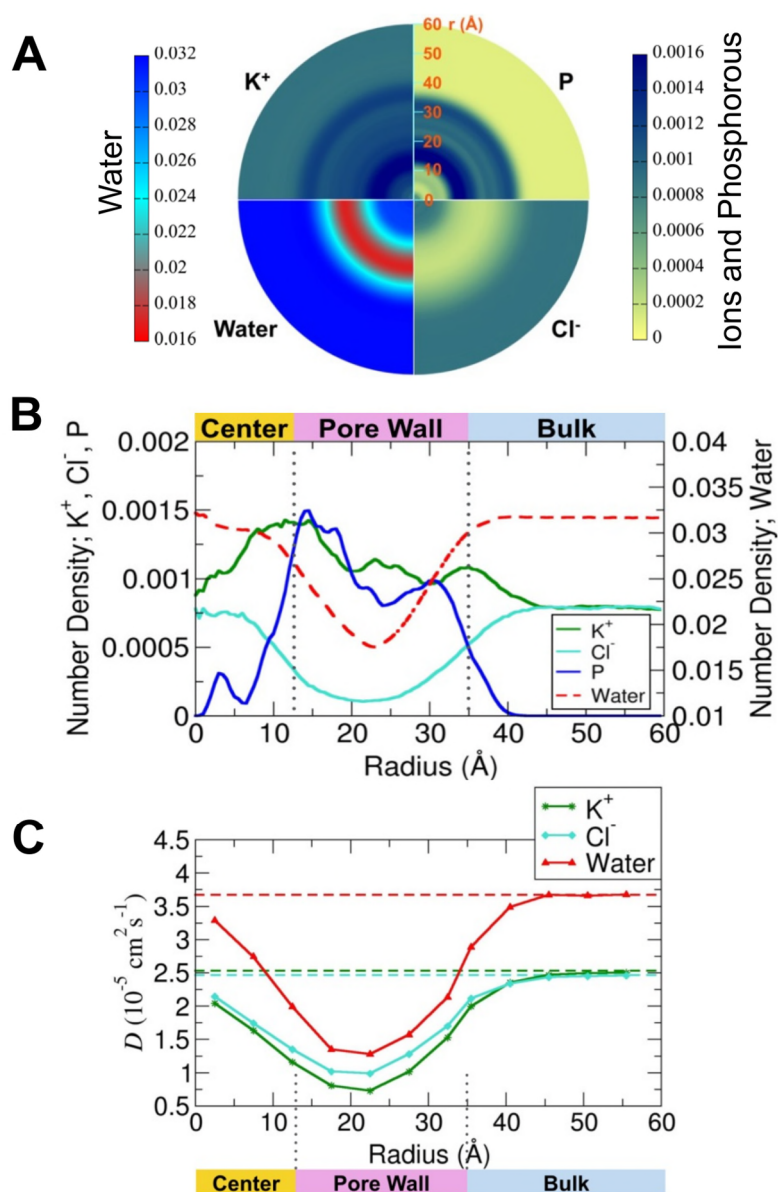
**Figure 6**: **Density and diffusion of ions and water through the DNT walls**.

**(A)** Radial distribution of phosphorous atoms, K$^+$ ions, Cl$^-$ ions and of water molecule densities. **(B)** Densities of phosphorous atoms, K$^+$ ions, Cl$^-$ ions and water molecules, as a function of the radial distance from the center of the DNT. The DNT pore wall extends ca. 12 to 35 Å along the radial axis. **A** and **B** were calculated using cylindrical grid shells of thickness 0.5 Å and length extending over the G2-G5 region of the DNT (see SI Methods and Fig. S2A). **(C)** Diffusion coefficients of K$^+$ ions, Cl$^-$ ions and water molecules as a function of the radial distance to the center of the DNT. The horizontal dashed lines show values corresponding to bulk conditions. The $D$ values were calculated in cylindrical grid shells of thickness 5 Å and G2-G5 length (see SI Methods).
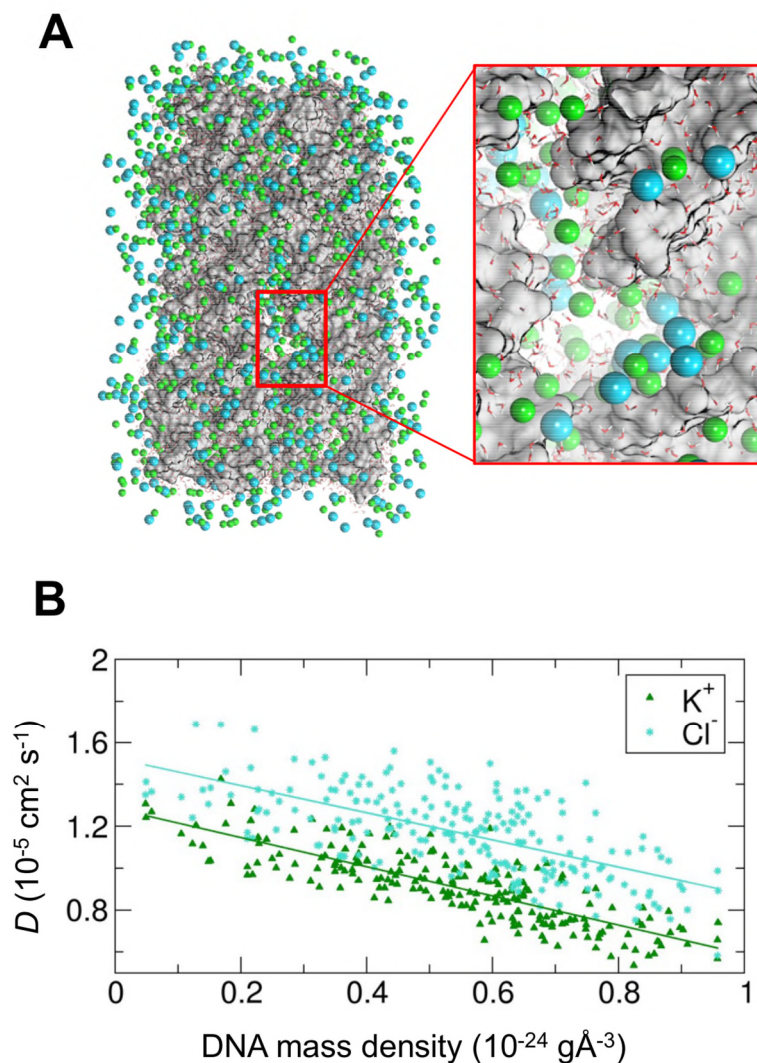
**A**



**B**



**Figure 7: Porous nature of the DNT walls.**

**(A)** Snapshot of the DNT1 simulation showing water molecules and ions within 15 Å of the DNT. The DNT is represented as grey surface, oxygen of water molecules as red points, $K^+$ ions as green spheres and $Cl^-$ ions as cyan spheres. The right inset shows a magnified leaky region of the DNT wall. **(B)** Scatter plot showing the local diffusion coefficients of $K^+$ ions (green triangles) and $Cl^-$ ions (cyan asterisks) as a function of the local mass density of DNA, calculated in each bin of the grid constructed along the pore wall in cylindrical coordinates (see SI Methods and Fig. S2B). The green and cyan solid lines represent linear regressions through the data points for $K^+$ and $Cl^-$, respectively (with correlation coefficients of -0.70 and -0.65, respectively).

**ToC Graphic**